Polymer 264 (2023) 125541

Contents lists available at ScienceDirect

Polymer

journal homepage: www.elsevier.com/locate/polymer

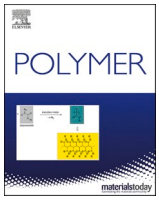

Constructing conjugated microporous polymers containing triphenylamine moieties for high-performance capacitive energy storage

Maha Mohamed Samy [a,b], Mohamed Gamal Mohamed [a,b,**], Santosh U. Sharma [c,d], Swetha V. Chaganti [c,d], Tharwat Hassan Mansoure [b], Jyh-Tsung Lee [c,d], Tao Chen [e], Shiao-Wei Kuo [a,f,*]

[a] Department of Materials and Optoelectronic Science, College of Semiconductor and Advanced Technology Research, Center for Functional Polymers and Supramolecular Materials, National Sun Yat-Sen University, Kaohsiung, 804, Taiwan
[b] Chemistry Department, Faculty of Science, Assiut University, Assiut 71515 , Egypt
[c] International PhD Program for Science, National Sun Yat-sen University, Kaohsiung, 80424, Taiwan
[d] Department of Chemistry, National Sun Yat-Sen University, Kaohsiung, 80424, Taiwan
[e] Ningbo Institute of Material Technology and Engineering, Chinese Academy of Science, Ningbo, 315201, China
[f] Department of Medicinal and Applied Chemistry, Kaohsiung Medical University, Kaohsiung, 807, Taiwan

ARTICLE INFO

Keywords:
Conjugated microporous polymers
Suzuki coupling
Triphenylamine
Porosity
Energy density
Supercapacitor

ABSTRACT

In this research we developed two triphenylamine (TPA)-linked conjugated microporous polymers (CMPs), TPA-TAB and TPA-TBN, through Suzuki couplings of tris(4-(4,4,5,5-tetramethyl-1,3,2-dioxaborolan-2-yl)phenyl) amine (TPA-BO) with the aryl bromides tetrakis(4-bromophenyl)benzidine (TAB-Br_4) and 2,7,10,15-tetrabromotetrabenzonaphthalene (TBN-Br_4), respectively. These CMPs, which have substantial surface surfaces and outstanding thermal stability, could be employed as electrode materials in supercapacitor (SC) devices. In a three-electrode SC, the TPA-TAB CMP exhibited ultrahigh specific capacitance (684 F g^{-1} at 0.5 A g^{-1}) and long-term stability, with a capacitance retention of 99.5% after 5000 cycles (at 10 A g^{-1}). Moreover, a two-electrode symmetric SC incorporating TPA-TAB CMP presented a capacitance of 117 F g^{-1} and a high retention of 98% when subjected to 5000 cycles at 10 A g^{-1}. This exceptional performance resulted from was achieved through the use of redox-active TPA units and a large BET surface area (490 m^2 g^{-1}). Accordingly, such TPA-CMPs appear to have promise for use in charge and energy storage applications.

1. Introduction

Using energy without damaging the environment will be an important issue in the future to maintain the health of all living creatures; accordingly, limiting the burning of fossil fuels and decreasing the emissions of carbon are necessary goals [1–4]. Indeed, much research has been conducted into the development of novel concepts for energy storage, rectification, and transport. Among the possible electrical energy storage devices, electrochemical capacitors and batteries appear to be particularly important systems for producing clean energy, due to their ability to transform chemical energy into electrical energy [5,6]. Supercapacitors (SCs) appear to be a sustainable alternative technology to batteries, fuel cells, and classical capacitors; they are attractive because of their long cycle life, high reliability, remarkable cycling stability, minimum environmental effect, low maintenance costs, pulsed power density, and fast charge/discharge rates [7–11]. Two main processes dominate the storage of energy in SCs: in electrical double-layer capacitors (EDLCs), by reversible ion adsorption through the interface of the electrode (e.g., porous carbon); in pseudocapacitors, by faradaic reactions that occur between the electrolyte and other organic moieties (e.g., conjugated polymers) or metal oxides [12–17]. Several recent reviews have highlighted the characteristics required for an effective SC electrode material: (i) interconnecting networks, to promote ion diffusion between particles; (ii) a conductive network, for ion percolation

* Corresponding author. Department of Materials and Optoelectronic Science, College of Semiconductor and Advanced Technology Research, Center for Functional Polymers and Supramolecular Materials, National Sun Yat-Sen University, Kaohsiung, 804, Taiwan.
** Corresponding author. Department of Materials and Optoelectronic Science, College of Semiconductor and Advanced Technology Research, Center for Functional Polymers and Supramolecular Materials, National Sun Yat-Sen University, Kaohsiung, 804, Taiwan.
E-mail addresses: mgamal.eldin12@yahoo.com (M. Gamal Mohamed), kuosw@faculty.nsysu.edu.tw (S.-W. Kuo).

https://doi.org/10.1016/j.polymer.2022.125541
Received 13 September 2022; Received in revised form 18 November 2022; Accepted 19 November 2022
Available online 21 November 2022

within the particles; (iii) uniform narrow micropores and a large surface area, to facilitate ion accumulation; and (iv) thickness and wettability, to improving the accessibility of effective sites [18–24].

Triphenylamine (TPA) derivatives are good electrode materials that can be processed into SC devices because of their high charge mobilities, excellent thermal stabilities, unique electronic properties, and high redox activity. Furthermore, the presence of TPA moieties as repeating radical units in, for example, polytriphenylamines (PTPAs) allows reversible radical redox reactions to occur through charge/discharge processes [25–27]. The chemical structures of the conjugated polymers are responsible for pseudocapacitive energy storage, while the microstructure and porosity of electrodes both contribute to a fast scan rate and EDLC behavior. Thus, a single conjugated polymer can be used to realize both types of energy storage; as such, they can be low-cost alternatives to the rare and expensive materials often employed in conventional SC devices [28].

Conjugated microporous polymers (CMPs) have been applied widely in the fields of catalysis, sensing, gas storage, and energy conversion, as well as in several energy storage applications [29–46]. CMPs are formed through covalent linkage of π-conjugated rigid subunits containing additional functionality, typically producing three-dimensional (3D) networks having micropores with diameters of less than 2 nm as well as high surface areas. These porous structures provide many opportunities for electron and ion transmission, a distinguishing feature that separates CMPs from other linear polymers. CMPs have frequently been constructed using common C–C coupling (Sonogashira, Yamamoto, and Suzuki) and oxidative polymerization strategies [47–50]. These coupling reactions often provide high degrees of polymerization and crosslinking and enable the introduction of a wide range of organic moieties. Accordingly, CMPs have become useful materials as electrodes in energy storage devices, with performance approaching that of other standard electrode materials [51,52]. For example, triazatruxene-based CMPs have exhibited capacitances between 141 and 183 F g^{-1} [53]; a poly(aminoanthraquinone) CMP provided a three-electrode capacitance of 576 F g^{-1} [54]; and thianthrene-based POPs have a capacitance of 217 F g^{-1} [55]. The quest remains, however, to develop less expensive and more effective conjugated microporous materials for use as electrodes in SC applications. Toward this goal, in this study, we employed simple Suzuki coupling between a TPA derivative (TPA-BO) and two aryl bromides (TAB-Br_4 and TBN-Br_4) to afford TPA-CMP networks (the TPA-TAB and TPA-TBN CMPs, respectively) that function as high-performance electrode materials for SCs.

2. Experimental

2.1. Materials

Sodium hydrogen carbonate ($NaHCO_3$), potassium acetate (KOAc), triphenylamine (TPA), N-bromosuccinimide (NBS), Pd(dppf)Cl_2, Pd(PPh_3)$_4$, magnesium sulfate anhydrous ($MgSO_4$) and trifluoromethanesulfonic acid (CF_3SO_3H) were purchased from Sigma-Aldrich. 2,3-Dichloro-5,6-dicyano-1,4-benzoquinone (DDQ), methane sulfonic acid (CH_3SO_3H), bis(pinacolato)diboron (B_2pin_2), dimethylformamide (DMF) and potassium carbonate (K_2CO_3), were ordered from Alfa Aesar. 1,4-dioxane was bought from Acros. The synthesis of tris(4-bromophenyl)amine (TPA-Br_3) was described in detail in the supporting information with their spectroscopic analyses [Scheme S1, Figs. S1–S3] [55].

2.2. Synthesis of monomers

2.2.1. Synthesis of Tris(4-(4,4,5,5-tetramethyl-1,3,2-dioxaborolan-2-yl) phenyl)amine (TPA-BO)

A mixture of TPA-Br_3 (3.0 mmol), B_2pin_2 (11 mmol), CH_3COOK (52 mmol), and Pd(dppf)Cl_2 (0.51 mmol) was heated in 1,4-dioxane at 80 °C for two days. After cooling, DI water was added and extracted with CH_2Cl_2. The combined extracts were dried ($MgSO_4$), filtered, and concentrated. A yellow solid was obtained after purification through chromatography with EtOAc/hexane (1:2) (Scheme S2). FTIR (Fig. S4): 2981, 1585, 1359, 1309, 1142 cm^{-1}. ^{1}H NMR (Fig. S5): 7.76, 7.05, 1.37 (s, 36H, CH_3) ppm. ^{13}C NMR (Fig. S6): 151, 136, 124, 123, 84, 23 ppm.

2.2.2. Synthesis of 4-bromo-N-(4-bromophenyl)-N-phenylaniline (TPA-Br_2)

A solution of TPA (5.00 g, 20.0 mmol) and NBS (7.23 g, 41.57 mmol) in DMF (70 mL) was kept stirring overnight. The mixture was extracted with H_2O and CH_2Cl_2. The organic layer was dried over $MgSO_4$. The resulting viscous oil was purified through column chromatography with hexane to give TPA-Br_2 (43%, Scheme S3). ^{1}H NMR [Fig. S7(a)]: 7.35–7.34 (4H), 7.28–7.26 (2H), 7.07–7.06 (3H), 6.94–6.93 (4H). ^{13}C NMR [Fig. S7(b)]: 115.39, 123.70, 124.56, 125.58, 129.50, 132.30, 146.49, 147.33.

2.2.3. Synthesis of tetrakis(4-bromophenyl)benzidine (TAB-Br_4)

Solution of methanesulfonic acid (CH_3SO_3H, 2 mL) and TPA-Br_2 (0.77 mmol) in dry CH_2Cl_2 (25 mL) at 0 °C was stirred for 1 h. DDQ (1.16 mmol) was added carefully to the mixture, which was then stirred for 12 h. Then, saturated $NaHCO_3$ (45 mL) was added, and the reaction was extracted with CH_2Cl_2. The residue was recrystallized by acetonitrile to give a white solid (41%, Scheme S3). FTIR (Fig. S8): 3031 (Ar–H), 1600 (C=C), 1276 (C–N), 717 (C–Br) cm^{-1}. ^{1}H NMR [Fig. S9 (a)]: 7.45–7.43 (2H), 7.37–7.35 (4H), 7.11–7.09 (2H), 6.99–6.97 (4H). ^{13}C NMR [Fig. S9(b)]: 146.34, 145.96, 135.45, 132.40, 127.65, 125.57, 124.53, 115.66.

2.2.4. Synthesis of 2,7,10,15-tetrabromotetrabenzonaphthalene (TBN-Br_4)

TPE-Br_4 (3.00 g, 4.6 mmol), 2,3-dichloro-5,6-dicyano-1,4-benzoquinone (2.50 g, 11 mmol) were put to dry DCM (235 mL) and then was allowed for cooling into ice around 1 h. Next, CF_3SO_3H (2.75 mL) was slowly added and kept stirring for 2 h at 0 °C. After that, the reaction was stirred at ambient temperature for 5 h. Then, methanol (55 mL) was poured into the flask and the reaction solution was stirred genteelly at ambient temperature overnight. The solid afforded was filtered off and washed exhaustively with different solvents (THF, methanol, and acetone) to give pale brown solid (1.87 g, 63%, Scheme S4). FT-IR (KBr, cm^{-1}, Fig. S10): 3079 (C–H aromatic), 566 (C–Br stretching). ^{1}H NMR (500 MHz, $CDCl_3$, δ, ppm, Fig. S11): 8.75 (d, 4H), 8.41 (d, 4H), 7.75 (dd, 4H).

2.2.5. Synthesis of TPA-CMPs

TBA-Br_4 (0.10 g, 0.12 mmol), TPA-BO (0.10 g, 0.16 mmol), K_2CO_3 (0.13 g, 0.95 mmol), and Pd catalyst (0.040 g, 0.030 mmol) in DMF (10 mL) and DI water (3 mL) was deoxygenated with N_2 gas for 30 min and the heated at 110 °C for 72 h. The resulting precipitated solid was washed with THF. The TPA-TAB CMP (78%) was obtained as a powder after drying at 70 °C. A similar procedure was applied to obtain the TPA-TBN CMP (81%), with TBN-Br_4 (0.10 g, 0.15 mmol) used instead of TBA-Br_4 (Scheme 1). Elemental analysis for TPA-TAB CMP: C, 88.55%; N, 5.36%. Elemental analysis for TPA-TBN CMP: C, 93.37%; N, 1.04%.

3. Results and discussion

3.1. Synthesis and structural investigation of the TPA-TAB and TPA-TBN CMPs

We used Suzuki coupling of the TPA-BO monomer with TAB-Br_4 and TBN-Br_4 to afford the TPA-TAB and TPA-TBN CMPs as insoluble solids, of green and gray appearance, respectively, in yields of 78 and 81%, respectively (Scheme 1). We employed Fourier transform infrared (FTIR) and solid-state ^{13}C NMR spectroscopy to characterize the structures of these TPA-CMPs. Bands representing the B–O bonds of TAP-BO (at 1309 cm^{-1}) and the C–Br bonds of the aryl bromide monomers (TBA-

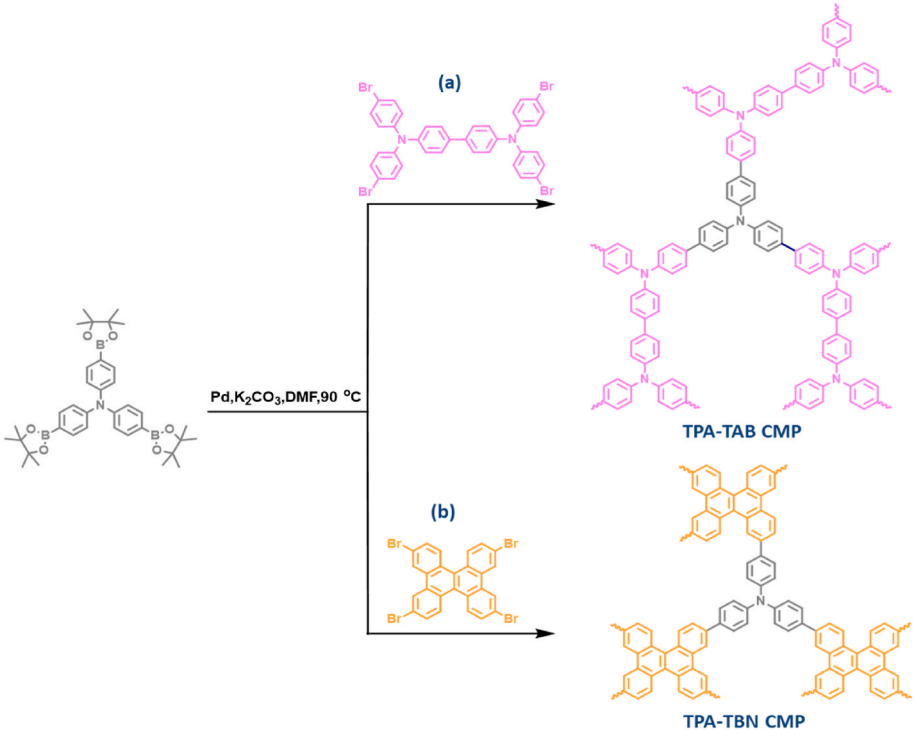

Scheme 1. Synthesis of the (a) TPA-TBA and (b) TPA-TBN CMPs.

Br_4 and TBN-Br_4; at 566 cm^{-1}) were absent in the FTIR spectra of the two TPA-CMPs [Fig. 1(a)]. Distinct bands were, however, present for their aromatic C═C and C–H bonds (ca. 1602, 1492, and 3031 cm^{-1}) and C–N bonds (ca. 1272 cm^{-1}). The solid-state ^{13}C NMR spectra of these two TPA-CMPs featured characteristic signals near 146 ppm and in the range 136.5–114.0 ppm, originating from the C–N and aryl units, respectively [Fig. 1(b)].

We employed thermogravimetric analysis (TGA) of the two TPA-CMPs, applying a heating rate of 20 °C min^{-1} under a N_2 environment. The TGA traces of the TPA-TAB and TPA-TBN CMPs revealed [Fig. 2(a)] high values of T_{d5} (ca. 335 and 404 °C, respectively) and T_{d10} (ca. 486 and 500 °C, respectively), with carbon residue of 74 and 70 wt %, respectively, after heating up to 800 °C (Table 1). As expected for microporous polymers, the two TPA-CMPs had amorphous appearances, with only a broad peak near 21° featuring in their powder X-ray diffraction patterns [Fig. 2(b)]. Moreover, N_2 adsorption/desorption studies at 77 K, performed after heating these TPA-CMPs at 150 °C to remove any residual solvent or moisture, demonstrated their microporosities. The TPA-TAB CMP provided a type IV isotherm and had a Brunauer–Emmet–Teller (BET) surface area of 490 m^2 g^{-1}, while the

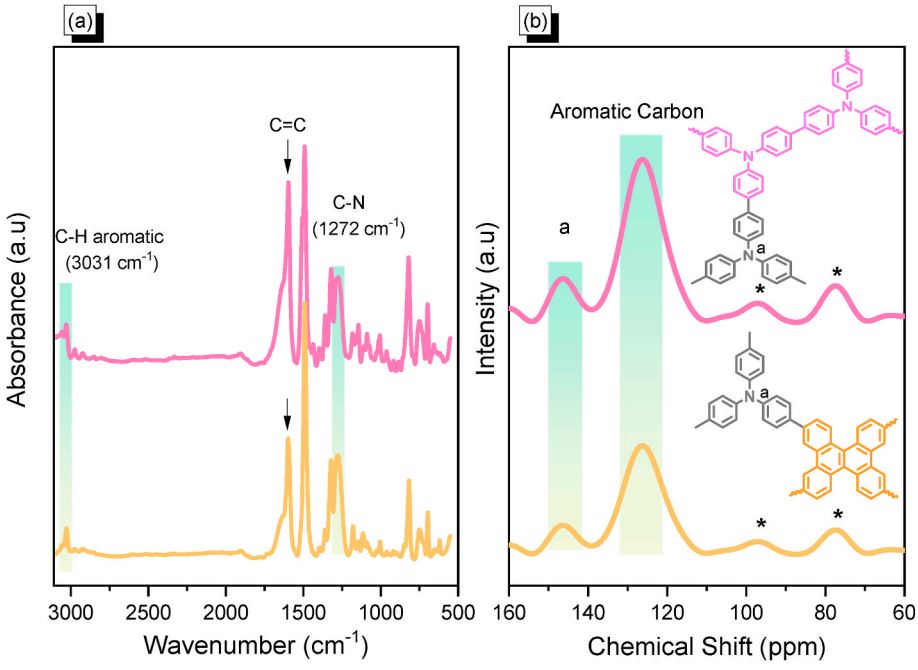

Fig. 1. (a) FTIR and (b) solid-state spectra of the TPA-TBA and TPA-TBN CMPs.

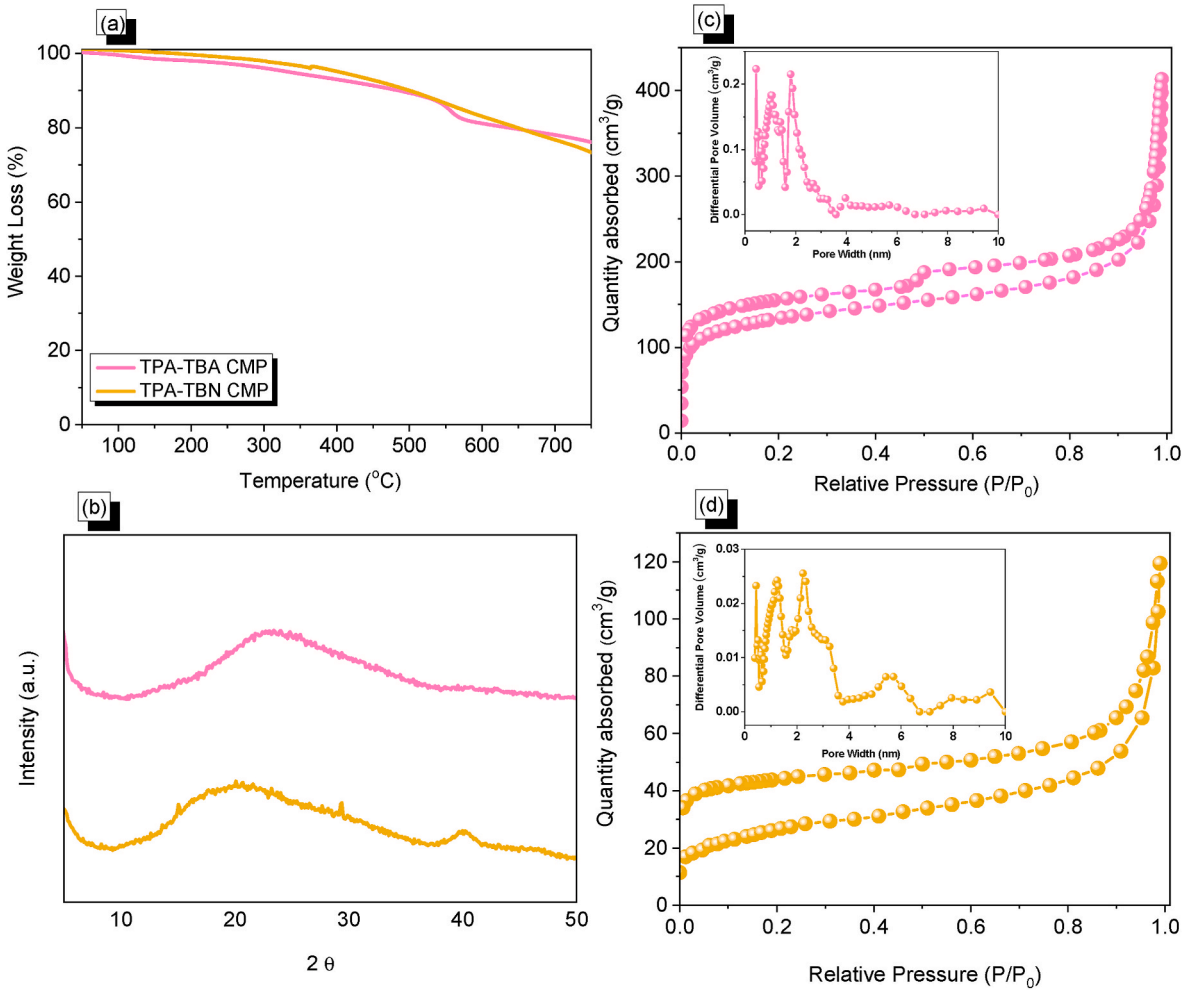

Fig. 2. (a) TGA, (b) XRD, (c) N_2 sorption isotherms, and (d) PSD profiles of the TPA-TBA and TPA-TBN CMPs.

Table 1
Presented BET and TGA data of the two TPA-CMPs.

Sample	T_{d5} (°C)	T_{d10} (°C)	Char yield (wt%)	Surface area ($m^2\ g^{-1}$)	Pore size (nm)
TPA-TAB CMP	335	486	74	490	0.45–3.98
TPA-TBN CMP	404	500	70	100	0.41–2.21

Table 2
Parameters determined from the fitted Nyquist plots of the TPA-CMPs.

Sample	R_s (Ω)	R_{ct} (Ω)	CPE–EDL ($S.s^n$)	CPE–P ($S.s^n$)
TPA-TAB CMP	31	252	0.0000933	0.0001870
TPA-TBN CMP	35	120	0.0027075	0.0001974

TPA-TBN CMP displayed a type III isotherm with a BET surface area of 100 $m^2\ g^{-1}$ [Fig. 2(c) and (d)]. Furthermore, we fitted the N_2 sorption isotherms by applying nonlocal density functional theory to simulate the pore size distributions (PSDs) of our two TPA-CMPs. The PSD curves of the TPA-TAB and TPA-TBN CMPs reflected the presence of micropores, as well as some mesopores, with diameters of 0.45–3.98 and 0.41–2.21 nm, respectively [Fig. 2(c) and (d); Table 1].

We used scanning electron microscopy (SEM) and transmission electron microscopy (TEM) to examine the morphologies of our CMPs. The SEM images of the TPA-TAB and TPA-TBN CMPs revealed interconnected aggregates of nanoparticles within their porous networks [Fig. 3(c) and (d)]. Also, TEM images of the two materials displayed sphere shapes [Fig. 3(a) and (b), and S12]. Elemental mapping, performed using energy dispersive spectroscopy (EDS), revealed the presence of C and N atoms throughout the TPA-CMP materials (Fig. 3, S13, and S14).

3.2. Electrochemical performance of the TPA-TAB and TPA-TBN CMPs

To analyze our prepared CMPs' electrochemical performance and assess their suitability as energy storage electrode materials, we performed cyclic voltammetry (CV) and galvanostatic (GCD) measurements, within the potential range from 0 to −1.0 V. Fig. 4(a) and **4(b)** displays the CV traces of the TPA-TAB and TPA-TBN CMPs recorded at various scan rates in the range 5–200 mV s^{-1}. A characteristic humped-rectangular form appeared in both cases and remained steady during scan sweeping, demonstrating that our TPA-CMPs were stable in these circumstances and that their capacitance arose from EDLC behavior [56, 57].

The CV traces also revealed that these materials had high-rate capabilities and underwent their redox processes with simple kinetics. The presence of the redox-active TPA moieties, containing electroactive N atoms attached to three phenyl rings, in the skeletons of the two TPA-CMPs afforded them the ability to exhibit reversible radical redox activity throughout the charge and discharge cycles. We also examined the GCD profiles and capacitances of these materials at current densities ranging from 0.5 to 5 A g^{-1} [Fig. 4(c) and **(d)**]. All of the GCD curves had

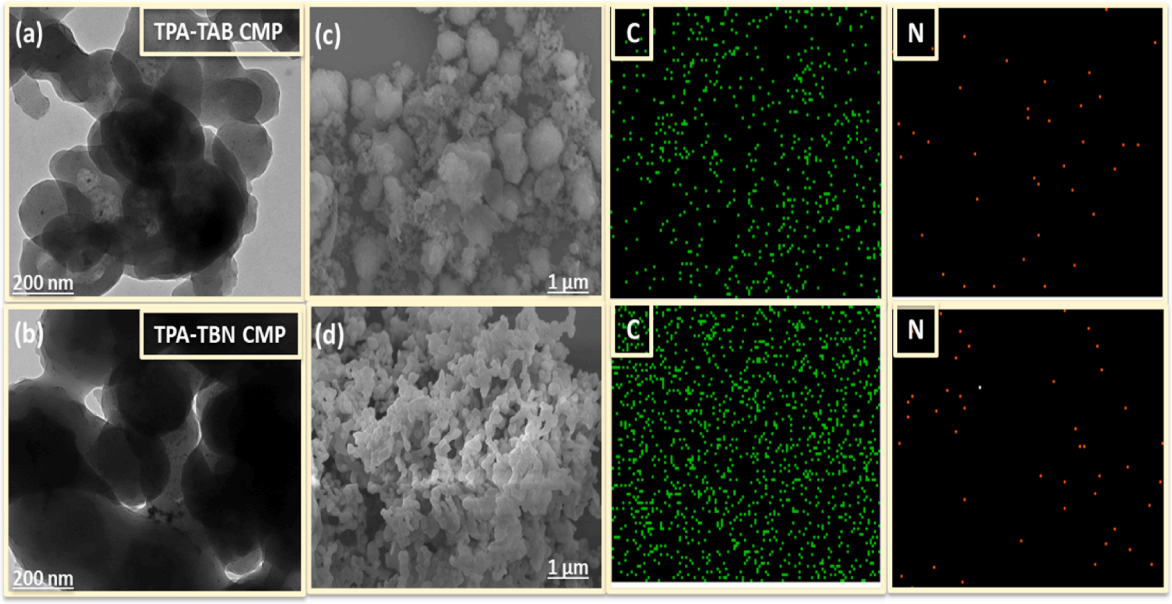

Fig. 3. (a, b) TEM and (c, d) SEM images of the (a, c) TPA-TAB and (b, d) TPA-TBN CMPs, and their EDS mapping images.

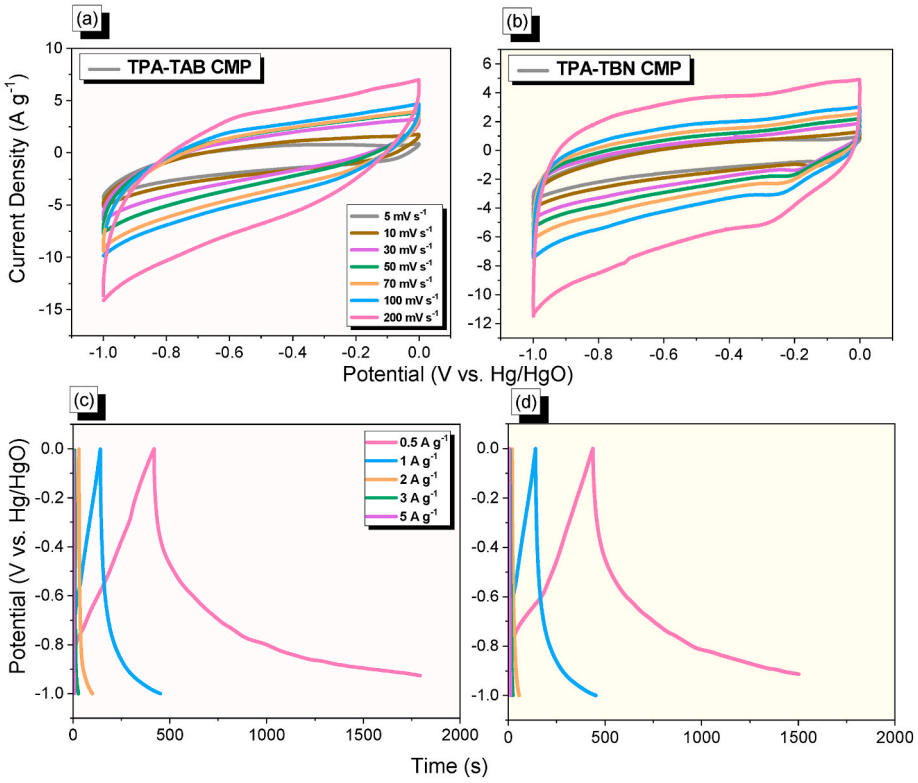

Fig. 4. (a, b) CV traces and (c, d) GCD curves of the (a, c) TPA-TAB and (b, d) TPA-TBN CMPs.

a bent-triangular form, indicating pseudocapacitive and EDLC properties. When comparing the charging and discharging periods for both materials, the discharge times were longer than the charging times, suggesting enhanced capacitance. Fig. 5(a) displays the measured specific capacitances. When TPA-CMPs samples measured at current densities of 0.5, 1, 2, 3, and 5 A g^{-1}, the TPA-TAB CMP delivered specific capacitances of 684, 311, 138, 59, and 26 F g^{-1}, respectively; for the TPA-TBN CMP, these values were 531, 310, 72, 42, and 31 F g^{-1}, respectively. Thus, the highest capacitance of the TPA-TAB CMP (684 F g^{-1}) was greater than that of the TPA-TBN CMP (531 F g^{-1}). We attribute this superior performance to the larger surface area (490 m^2 g^{-1}) and extra N heteroatom of the TPA-TAB CMP, both of which would accelerate the movement of electrolyte ions to the electrode surface to achieve the redox process. To examine the stability of these CMPs, we investigated their cycle stability over 5000 cycles at 10 A g^{-1} [Fig. 5(b)]. Here, the TPA-TAB and TPA-TBN CMPs exhibited outstanding capacity retentions of 99.5 and 96%, respectively. Such long-term stability suggested that these CMPs might be suitable for real electrochemical energy

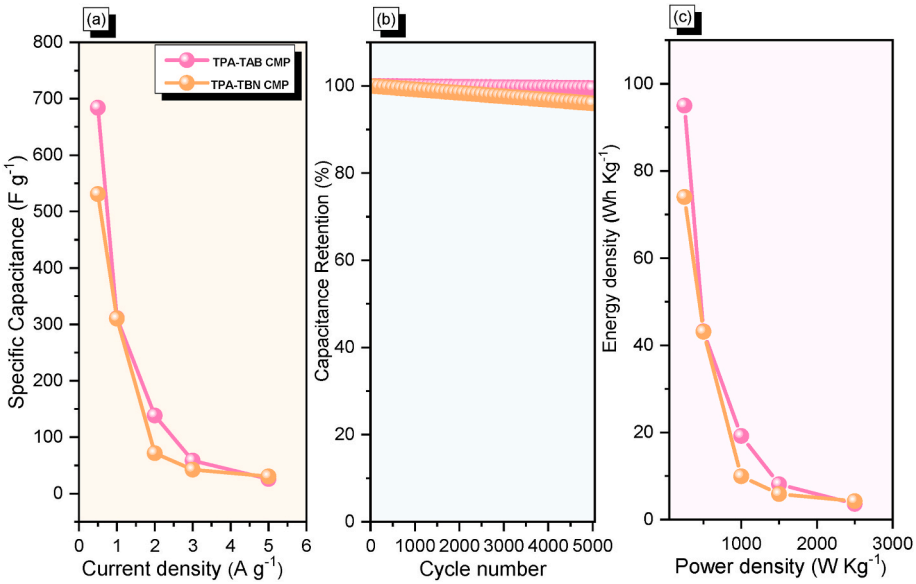

Fig. 5. (a) Specific capacitances, (b) long-term cycling stability profiles, and (c) Ragone plots of the TPA-TAB and TPA-TBN CMPs.

storage applications. In addition, the TPA-TAB and TPA-TBN CMPs delivered energy densities of 95 and 74 W h kg^{-1}, respectively [Fig. 5 (c)]. Notably, our TPA-CMPs exhibited ultrahigh performance (capacitance and stability) when compared with other previously reported CMPs in three-electrode SCs (Table S1).

Fig. 6(a) presents the Nyquist plots of our CMPs, determined using electrochemical impedance spectroscopy (EIS), with a fitted equivalent electric circuit containing a series resistance (R_s), charge transfer resistance (R_{ct}), constant phase elements representing EDLC (CPE–EDL) and pseudocapacitive (CPE–P) behavior, and a Warburg element (Z_w), as displayed in Fig. 6(b). The plot of the TPA-TAB CMP cell featured a shorter straight line than that of the TPA-TBN CMP cell; furthermore, the line for the TPA-TAB CMP cell was leaning toward the vertical Z'' axis, indicating that it had a high capacitive performance. The Warburg length/resistance of the TPA-TBN CMP was higher than that of the TPA-TAB CMP, as evidenced by the straight line deviating from the vertical axis. The TPA-TAB and TPA-TBN CMPs had ohmic resistances of 31 and 35 Ω [Table 2], respectively, and charge transfer resistances of 252 and 120 Ω [Table 2], respectively. Fig. 6(c) displays their frequency-dependent magnitude Bode plots. At low frequencies, we observed slanted lines with a negative slope, while at high frequencies, less resistance was observed, validating the remarkable capacitive

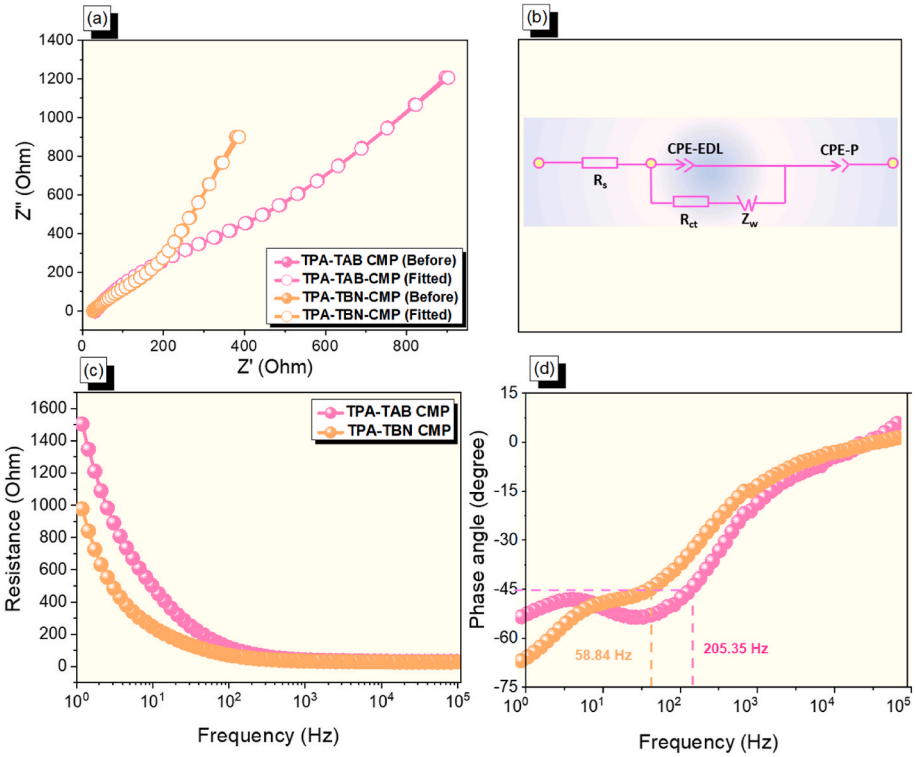

Fig. 6. (a) Nyquist plots, (b) fitted circuit, (c) Bode plots of frequency with respect to magnitude of resistance, and (d) Bode plots of the frequency with respect to phase angle (to determine knee frequencies) for the TPA-TAB and TPA-TBN CMPs.

characteristics of these electrode materials. Fig. 6(d) provides plots of the frequency-dependent phase angles for these CMP electrodes. The knee frequencies were determined at a phase angle of −45°, at which point the electrode's resistive and capacitive characteristics were equal. The knee frequency is a well-established indication of a compound's rate capacity [61]. The TPA-TAB and TPA-TBN CMPs had knee frequencies of 205.35 and 58.84 Hz, respectively.

For a deeper study of the possible practical application of our TPA-CMPs as SC electrodes, we evaluated the electrochemical functionality of symmetric SC devices in the form of CR2032 coin cells. Here, our CMPs served as both the cathode and anode within symmetric supercapacitors (SSCs). We recorded CV profiles at various scan speeds [Fig. 7 (a) and **7(b)**] and GCD curves at various current densities [Fig. 7(c) and **7(d)**]. The cyclic voltammograms of both materials possessed almost-rectangular shapes, the sign of a SC. Because higher scan rates produced larger current densities, demonstrating improved kinetics and rate capacities, we inferred that the electrode integrity was maintained even at higher scan rates. The GCD curves of the TPA-TAB and TPA-TBN CMPs were of approximately triangular form, with minimal bending occurring during charging, suggesting a combination of pseudocapacitive and EDLC behavior.

In addition, the discharging time was longer than the charging time, implying that both CMPs might be suitable for real-world use. The discharge time for the TPA-TAB CMP was almost twice that of the TPA-TBN CMP, suggesting that the capacity of the former would be more than twice that of the latter; this behavior was confirmed from the capacity graph displayed in Fig. 8(a). Furthermore, when operated at current densities of 0.5, 1, 2, 3, and 5 A g^{-1}, the coin cell incorporating the TPA-TAB CMP displayed specific capacitances of 117, 167, 86, 60, and 37 F g^{-1}, respectively; for the TPA-TBN CMP, these values were 100, 79, 36, 28, and 25 F g^{-1}, respectively. When we performed cycle stability tests for the TPA-CMPs over 5000 cycles at 10 A g^{-1} [Fig. 8(b)], the TPA-TAB and TPA-TBN CMPs provided capacity retentions of 98 and 93%, respectively, confirming their long-term stabilities. In addition, the TPA-TAB and TPA-TBN CMPs achieved energy densities of 17 and 13 W h kg^{-1}, at a power density of 125 W kg^{-1}, respectively, as determined from the Ragone plot diagram in Fig. 8(c).

These values are among the highest ever reported for SSC devices (Fig. 9); for example, PANI/NCNT composite [58], MCSF porous material [59], and IHPNC- carbon nanotubes [60] offered an energy density of 11.1, 9.6 and 8.7 Wh kg^{-1} at 980, 108.5 and 195 W kg^{-1}, respectively. N-PCNFs/PSN presented an energy density of 8.5 Wh kg^{-1} for a power density = 250 W kg^{-1} [61]; N-CNFs/900 displayed an energy density of 7.11 Wh kg^{-1} at 125 W kg^{-1} [62]; and FC-CMPs/rGO delivered a power density of 8 Wh kg^{-1} at 124 W kg^{-1} [63]. Furthermore, we demonstrated the practical application of our TPA-CMPs as symmetric cells through their use in the illumination of a light-emitting diode (LED; Fig. S15).

4. Conclusion

We have prepared two TPA-based CMPs through single-step Suzuki couplings. These TPA-TAB and TPA-TBN CMPs possessed exceptional thermal stabilities (T_{d10} > 400 °C), large surface areas, and outstanding performance for energy storage, arising from their chemical structures featuring redox-active TPA units. In particular, the TPA-TAB CMP exhibited three-electrode capacitance of 684 F g^{-1} and long-term stability (99.5%) after 5000 cycles. Moreover, it demonstrated a two-electrode SSC capacitance of 117 F g^{-1} and high-capacity retention of 98% after 5000 cycles. Thus, these TPA-CMPs appear to be attractive electroactive materials for application as active electrodes in electrochemical energy storage devices.

CRediT authorship contribution statement

Maha Mohamed Samy: Conceptualization, Data curation, Writing – original draft. **Mohamed Gamal Mohamed:** Conceptualization, Methodology, Formal analysis, Data curation, Supervision, Writing – original draft. **Santosh U. Sharma:** Data curation, Writing – original draft. **Swetha V. Chaganti:** Conceptualization. **Tharwat Hassan Mansoure:**

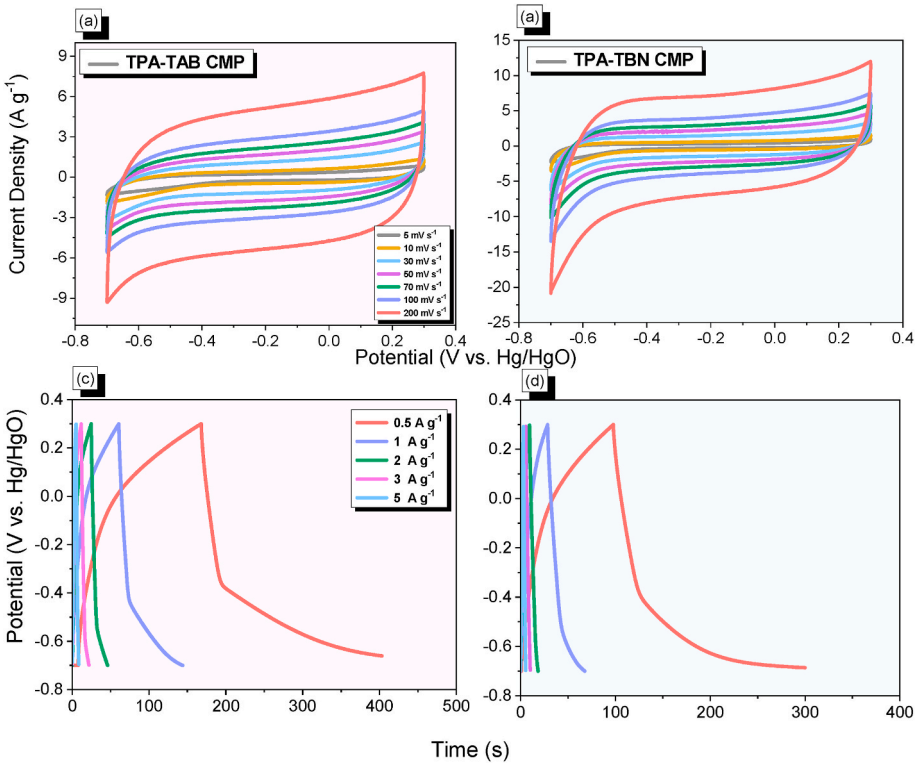

Fig. 7. (a, b) CV traces and (c, d) GCD curves of SSC coin cells incorporating the (a, c) TPA-TAB and (b, d) TPA-TBN CMPs.

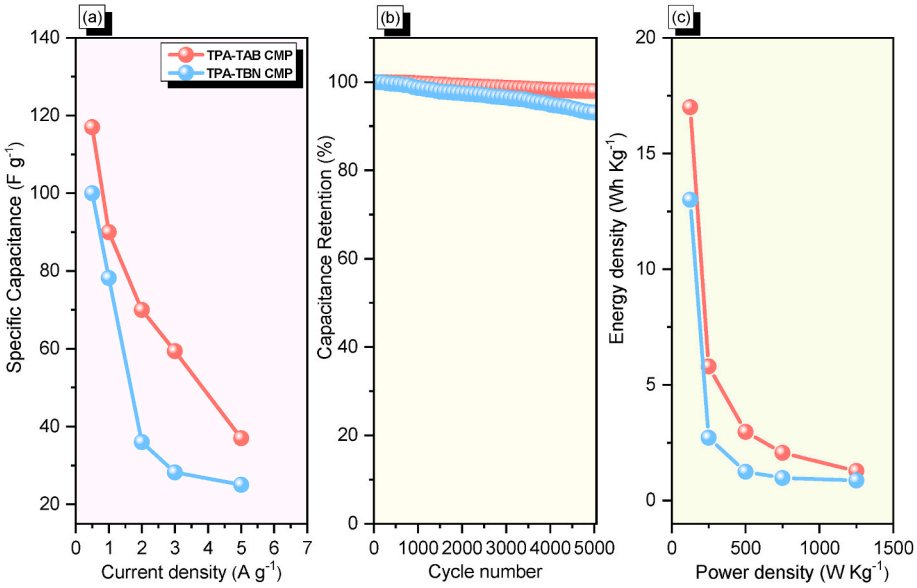

Fig. 8. (a) Specific capacitances, (b) long-term cycling stability profiles, and (c) Ragone plots of SSC coin cells incorporating the TPA-TAB and TPA-TBN CMPs.

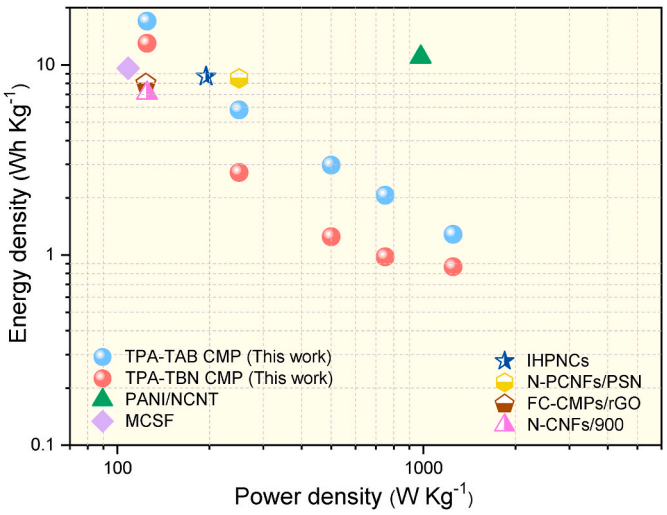

Fig. 9. Ragone plots of SSC devices incorporating the TPA-TAB and TPA-TBN CMPs, compared with those of other previously reported SSC devices.

Conceptualization. **Jyh-Tsung Lee:** Data curation. **Tao Chen:** Data curation. **Shiao-Wei Kuo:** Funding acquisition, Project administration, Supervision.

Declaration of competing interest

The authors declare that they have no known competing financial interests or personal relationships that could have appeared to influence the work reported in this paper.

Data availability

No data was used for the research described in the article.

Acknowledgments

This study was supported financially by the Ministry of Science and Technology, Taiwan, under contractsNSTC 110-2124-M-002-013 and 111-2223-E-110-004. The authors thank the staff at National Sun Yat-sen University for their assistance with the TEM (ID: EM022600) experiments.

Appendix A. Supplementary data

Supplementary data to this article can be found online at https://doi.org/10.1016/j.polymer.2022.125541.

References

[1] N.N. Loganathan, V. Perumal, B.R. Pandian, R. Atchudan, T.N.J. I Edison, M. Ovinis, Recent studies on polymeric materials for supercapacitor development, J. Energy Storage 49 (2022), 104149.
[2] M.G. Mohamed, T.H. Mansoure, M.M. Samy, Y. Takashi, A.A.K. Mohammed, T. Ahamad, S.M. Alshehri, J. Kim, B.M. Matsagar, K.C.-W. Wu, S.W. Kuo, Ultrastable conjugated microporous polymers containing benzobisthiadiazole and pyrene building blocks for energy storage applications, Molecules 27 (2022) 2025.
[3] S. Xiong, J. Liu, Y. Wang, X. Wang, J. Chu, R. Zhang, M. Gong, B. Wu, Solvothermal synthesis of triphenylamine-based covalent organic framework nanofibers with excellent cycle stability for supercapacitor electrodes, J. Appl. Polym. Sci. 139 (2022), 51510.
[4] M.M. Samy, M.G. Mohamed, A.F.M. El-Mahdy, T.H. Mansoure, K.C.W. Wu, S. W. Kuo, High-performance supercapacitor electrodes prepared from dispersions of tetrabenzonaphthalene-based conjugated microporous polymers and carbon nanotubes, ACS Appl. Mater. Interfaces 13 (2021) 51906–51916, https://doi.org/10.1021/acsami.1c05720.
[5] M.G. Mohamed, S.V. Chaganti, S.U. Sharma, M.M. Samy, M. Ejaz, J.T. Lee, K. Zhang, S.W. Kuo, Constructing conjugated microporous polymers containing the pyrene-4,5,9,10-tetraone unit for energy storage, ACS Appl. Energy Mater. 5 (2022) 10130–10140, https://doi.org/10.1021/acsaem.2c01842.
[6] S. Zheng, Q. Li, H. Xue, H. Pang, Q. Xu, A highly alkaline stable metal oxide@ metal-organic framework composite for high performance electrochemical energy storage, Natl. Sci. Rev. 7 (2020) 305–314.
[7] S. Liu, L. Kang, J. Henzie, J. Zhang, J. Ha, M.A. Amin, M.S.A. Hossain, S.C. Jun, Y. Yamauchi, Recent advances and perspectives of battery-type Anode materials for potassium ion storage, ACS Nano 15 (2021) 18931–18973.
[8] M.G. Mohamed, S.U. Sharma, N.Y. Liu, T.H. Mansoure, M.M. Samy, S.V. Chaganti, Y.L. Chang, J.T. Lee, S.W. Kuo, Ultrastable covalent triazine organic framework based on anthracene moiety as platform for high-performance carbon dioxide adsorption and supercapacitors, Int. J. Mol. Sci. 23 (2022) 3174.
[9] N.S. Shaikh, S.B. Ubale, V.J. Mane, J.S. Shaikh, V.C. Lokhande, S. Praserthdam, C. D. Lokhande, P. Kanjanaboos, Novel electrodes for supercapacitor: conducting polymers, metal oxides, chalcogenides, carbides, nitrides, MXenes, and their composites withgraphene, J. Alloys Compd. 893 (2022), 161998.
[10] S. Liu, L. Kang, J. Zhang, S.C. Jun, Y. Yamauchi, Carbonaceous anode materials for non-aqueous sodium- and potassium-ion hybrid capacitors, ACS Energy Lett. 6 (2021) 4127–4154.
[11] S. Zheng, Y. Sun, H. Xue, P. Braunstein, W. Huang, H. Pang, Dual-ligand and hard-soft-acid-base strategies to optimize metalorganic framework nanocrystals for stable electrochemical cyclingperformance, Natl. Sci. Rev. 9 (2021) nwab197.

[12] Y. Bai, C. Liu, T. Chen, W. Li, S. Zheng, Y. Pi, Y. Luo, H. Pang, MXene-copper/Cobalt hybrids via lewis acidic molten salts etching for high performance symmetric supercapacitors, Angew. Chem., Int. Ed. 60 (2021) 25318–25322.

[13] S. Liu, L. Kang, J. Zhang, E. Jung, S. Lee, S.C. Jun, Structural engineering and surface modification of MOF-derived cobalt-based hybrid nanosheets for flexible solid-state supercapacitors, Energy Storage Mater. 32 (2020) 167–177.

[14] Y. Tan, C. Xu, G. Chen, Z. Liu, M. Ma, Q. Xie, N. Zheng, S. Yao, Synthesis of ultrathin nitrogen-doped graphitic carbon nanocages as advanced electrode materials for supercapacitor, ACS Appl. Mater. Interfaces 5 (2013) 2241–2248.

[15] P. Kanninen, N.D. Luong, L.H. Sinh, I.V. Anoshkin, A. Tsapenko, J. Seppälä, A. G. Nasibulin, T. Kallio, Transparent and flexible high-performance supercapacitors based on single-walledcarbon nanotube films, Nanotechnology 27 (2016), 235403.

[16] M.G. Mohamed, M.M. Samy, T.H. Mansoure, S.U. Sharma, M.S. Tsai, J.H. Chen, J.-T. Lee, S.W. Kuo, Dispersions of 1,3,4-oxadiazole-linked conjugated microporous polymers withCarbon nanotubes as a high-performance electrode for supercapacitors, ACS Appl. Energy Mater. 5 (2022) 3677–3688.

[17] S. Liu, L. Kang, J. Hu, E. Jung, J. Zhang, S.C. Jun, Y. Yamauchi, Unlocking the potential of oxygen-deficient copper doped Co_3O_4 nanocrystals confined in carbon as an advanced electrode for flexible solid-state supercapacitors, ACS Energy Lett. 6 (2021) 3011–3019.

[18] J. Zhao, H. Lai, Z. Lyu, Y. Jiang, K. Xie, X. Wang, Q. Wu, L. Yang, Z. Jin, Y. Ma, J. Liu, Z. Hu, Hydrophilic hierarchical nitrogen-doped carbon nanocages for ultrahigh supercapacitive performance, Adv. Mater. 27 (2015) 3541.

[19] D. Kim, J. Kang, B. Yan, K.D. Seong, Y. Piao, Ambient temperature synthesis of iron-doped porous nickel pyrophosphate nanoparticles with long-term chemical stability for high-performance oxygen evolution reaction catalysis and supercapacitors, ACS Sustainable Chem. Eng. 8 (2020) 2843–2853.

[20] H. Zhao, J. Wang, Y. Zheng, J. Li, X. Han, G. He, Y. Du, Organic thiocarboxylate electrodes for a room-temperature sodium ion battery delivering an ultrahigh capacity, Angew. Chem., Int. Ed. 56 (2017) 15334–15338.

[21] M.G. Mohamed, A.F.M. EL-Mahdy, M.M.M. Ahmed, S.W. Kuo, Direct synthesis of microporous bicarbazole-based covalent triazine frameworks for high-performance energy storage and carbon dioxide uptake, ChemPlusChem 84 (2019) 1767–1774.

[22] W. Lyu, C. Yan, Z. Chen, J. Chen, H. Zuo, L. Teng, H. Liu, L. Wang, Y. Liao, Spirobifluorene-based conjugated microporous polymer-grafted carbon nanotubes for efficient supercapacitive energy storage, ACS Appl. Energy Mater. 5 (2022) 3706–3714.

[23] Y. Wang, W. Li, L. Zhang, X. Zhang, B. Tan, J. Hao, J. Zhang, X. Wang, Q. Hu, X. Lu, Amorphous cobalt hydrogen phosphate nanosheets with remarkable electrochemical performances as advanced electrode for supercapacitors, J. Power Sources 449 (2020), 227487.

[24] W. Septiani, N.L. Kaneti, Y.V. Fathoni, K.B. Wang, J. Ide, Y. Yuliarto, B. Nugraha, H.K. Dipojono, A.K. Nanjundan, D. Golberg, Y. Bando, Y. Yamauchi, Self-assembly of nickel phosphate-based nanotubes into two-dimensional crumpled sheet-like architectures for high-performance asymmetric supercapacitors, Nano Energy 67 (2020), 104270.

[25] A.F.M. El-Mahdy, M.G. Mohamed, T.H. Mansoure, H.H. Yu, T. Chen, S.W. Kuo, Ultrastable tetraphenyl-p-phenylenediamine based covalent organic frameworks as platforms for high-performance electrochemical supercapacitors, Chem. Commun. 55 (2019), 14890.

[26] C. Su, H. He, L. Xu, K. Zhao, C. Zheng, C. Zhang, A mesoporous conjugated polymer based on a high free radical density polytriphenylamine derivative: its preparation and electrochemical performance as a cathode material for Li-ion batteries, J. Mater. Chem. A 5 (2017) 2701.

[27] S. Wang, Y. Liu, Y. Ye, X. Meng, J. Du, X. Song, Z. Liang, Ultrahigh volatile iodine capture by conjugated microporous polymer based on N, N, N′, N′-tetraphenyl-1, 4-phenylenediamine, Polym. Chem. 10 (2019) 2608–2615.

[28] M.E. Roberts, D.R. Wheeler, B.B. McKenzie, B.C. Bunker, High specific capacitance conducting polymer supercapacitor electrodes based on poly(tris (thiophenylphenyl)amine), J. Mater. Chem. 19 (2009) 6977.

[29] M.M. Samy, M.G. Mohamed, T.H. Mansoure, T.S. Meng, M.A.R. Khan, C.C. Liaw, S. W. Kuo, Solid state chemical transformations through ring-opening polymerization of ferrocene-based conjugated microporous polymers in host–guest complexes with benzoxazine-linked cyclodextrin, J. Taiwan Inst. Chem. Eng. 123 (2022), 104110, https://doi.org/10.1016/j.jtice.2021.10.010.

[30] M. Ejaz, M.G. Mohamed, S.U. Sharma, J.T. Lee, C.F. Huang, T. Chen, S.W. Kuo, An ultrastable porous polyhedral oligomeric silsesquioxane/tetraphenylthiophene hybrid as a high-performance electrode for supercapacitors, Molecules 27 (2022) 6238, https://doi.org/10.3390/molecules27196238.

[31] M.G. Mohamed, T.C. Chen, S.W. Kuo, Solid-state chemical transformations to enhance gas capture in benzoxazine-linked conjugated microporous polymers, Macromolecules 54 (2021) 5866–5877, https://doi.org/10.1021/acs.macromol.1c00736.

[32] M.G. Mohamed, A.F.M. EL-Mahdy, M.G. Kotp, S.W. Kuo, Advances in porous organic polymers: syntheses, structures, and diverse applications, Mater. Adv. 3 (2022) 707–733, https://doi.org/10.1039/D1MA00771H.

[33] M.G. Mohamed, H.Y. Hu, M. Madhu, M. Ejaz, S.U. Sharma, W.L. Tseng, M. M. Samy, C.W. Huang, J.T. Lee, S.W. Kuo, Construction of ultrastable conjugated microporous polymers containing thiophene and fluorene for metal ion sensing and energy storage, Micromachines 13 (2022) 1466, https://doi.org/10.3390/mi13091466.

[34] M.G. Mohamed, M.M. M Ahmed, W.T. Du, S.W. Kuo, Meso/microporous carbons from conjugated hyper-crosslinked polymers based on tetraphenylethene for high-performance CO_2 capture and supercapacitor, Molecules 26 (2021) 738, https://doi.org/10.3390/molecules26030738.

[35] T.H. Weng, M.G. Mohamed, S.U. Sharma, S.V. Chaganti, M.M. Samy, J.T. Lee, S. W. Kuo, Ultrastable three-dimensional triptycene- and tetraphenylethene-conjugated microporous polymers for energy storage, ACS Appl. Energy Mater. (2022), https://doi.org/10.1021/acsaem.2c02809.

[36] M.G. Mohamed, N.Y. Liu, A.F.M. EL-Mahdy, S.W. Kuo, Ultrastable luminescent hybrid microporous polymers based on polyhedral oligomeric silsesquioxane for CO_2 uptake and metal ion sensing, Microporous Mesoporous Mater. 311 (2021), 110695, https://doi.org/10.1016/j.micromeso.2020.110695.

[37] C. Zhang, Y. Qao, P.X. Xiong, W.Y. Ma, P.X. Bai, X. Wang, Q. Li, J. Zhao, Y.F. Xu, Y. Chen, J.H. Zeng, F. Wang, Y.H. Xu, J.X. Jiang, Conjugated microporous polymers with tunable electronic structure for high-performance potassium-ion batteries, ACS Nano 13 (2019) 745–754.

[38] M.G. Mohamed, M.Y. Tsai, C.F. Wang, C.F. Huang, M. Danko, L. Dai, T. Chen, S. W. Kuo, Multifunctional polyhedral oligomeric silsesquioxane (POSS) based hybrid porous materials for CO_2 uptake and iodine adsorption, Polymers 13 (2021) 221, https://doi.org/10.3390/polym13020221.

[39] P.Y. Ju, S.J. Wu, Q. Su, X.D. Li, Z.Q. Liu, G.H. Li, Q.L. Wu, Salen-porphyrin-based conjugated microporous polymer supported Pd nanoparticles: highly efficient heterogeneous catalysts for aqueous C-C coupling reactions, J. Mater. Chem. A. 7 (2019) 2660–2666, https://doi.org/10.1039/C8TA11330K.

[40] M.G. Mohamed, T.H. Mansoure, Y. Takashi, M.M. Samy, T. Chen, S.W. Kuo, Ultrastable porous organic/inorganic polymers based on polyhedral oligomeric silsesquioxane (POSS) hybrids exhibiting high performance for thermal property and energy storage, Microporous Mesoporous Mater. 328 (2021), 111505, https://doi.org/10.1016/j.micromeso.2021.111505.

[41] Y.Y. Dai, W.J. Li, Z.X. Chen, X.G. Zhu, J.L. Liu, R.Y. Zhao, D.S. Wright, A. Noori, M. F. Mousavi, C. Zhang, An air-stable electrochromic conjugated microporous polymer as an emerging electrode material for hybrid energy storage systems, J. Mater. Chem. A. 7 (2019) 16397–16405, https://doi.org/10.1039/C9TA03001H.

[42] M.G. Mohamed, W.C. Chen, A.F.M. El-Mahdy, S.W. Kuo, Porous organic/inorganic polymers based on double-decker silsesquioxane for high-performance energy storage, J. Polym. Res. 28 (2021) 219, https://doi.org/10.1007/s10965-021-02579-x.

[43] W. Zeng, Y. Zhang, X.B. Zhao, M.L. Qin, X.Y. Li, W.S. Jin, D.Q. Zhang, One-pot synthesis of conjugated microporous polymers based on extended molecular graphenes for hydrogen storage, Polymer 174 (2019) 96–100, https://doi.org/10.1016/j.polymer.2019.04.069.

[44] M.M. Samy, I.M.A. Mekhemer, M.G. Mohamed, M.H. Elsayed, K.H. Lin, Y.K. Chen, T.L. Wu, H.H. Chou, S.W. Kuo, Conjugated microporous polymers incorporating Thiazolo[5,4-d]thiazole moieties for Sunlight-Driven hydrogen production from water, Chem. Eng. J. 446 (2022), 137158.

[45] W. Zhang, H. Zuo, Z. Cheng, Y. Shi, Z. Guo, N. Meng, A. Thomas, Y. Liao, Macroscale conjugated microporous polymers: controlling versatile functionalities over several dimensions, Adv. Mater. 34 (2022), 2104952, https://doi.org/10.1002/adma.202104952.

[46] M.M. Samy, M.G. Mohamed, S.W. Kuo, Pyrene-functionalized tetraphenylethylene polybenzoxazine for dispersing single-walled carbon nanotubes and energy storage, Compos. Sci. Technol. 199 (2020), 108360, https://doi.org/10.1016/j.compscitech.2020.108360.

[47] J. Schmidt, M. Werner, A. Thomas, Conjugated microporous polymer networks via Yamamoto polymerization, Macromolecules 42 (2009) 4426–4429.

[48] M.G. Mohamed, M.H. Elsayed, A.M. Elewa, A.F.M. EL-Mahdy, C.H. Yang, A.A. K. Mohammed, H.H. Chou, S.W. Kuo, Pyrene-containing conjugated organic microporous polymers for photocatalytic hydrogen evolution from water, Catal. Sci. Technol. 11 (2021) 2229–2241, https://doi.org/10.1039/D0CY02482A.

[49] S. Fischer, A. Schimanowitz, R. Dawson, I. Senkovska, S. Kaskel, A. Thomas, Cationic microporous polymer networks by polymerisation of weakly coordinating cations with CO2-storage ability, J. Mater. Chem. A 2 (2014) 11825–11829.

[50] M.M. Samy, S.U. Sharma, M.G. Mohamed, A.A.K. Mohammed, S.V. Chaganti, J. T. Lee, S.W. Kuo, Conjugated microporous polymers containing ferrocene units for high carbon dioxide uptake and energy storage, Mater. Chem. Phys. 287 (2022), 126177, https://doi.org/10.1016/j.matchemphys.2022.126177.

[51] N. Meng, H. Li, Y. Liu, Y. Liao, Self-templating synthesis of nitrogen-rich porous carbons using pyridyl functionalized conjugated microporous polytriphenylamine for electrochemical energy storage, Electrochim. Acta 402 (2022), 139531.

[52] M.G. Mohamed, E.C. Atayde Jr., B.M. Matsagar, J. Na, Y. Yamauchi, K.C.W. Wu, S. W. Kuo, Construction hierarchically mesoporous/microporous materials based on block copolymer and covalent organic framework, J. Taiwan Inst. Chem. Eng. 112 (2020) 180–192, https://doi.org/10.1016/j.jtice.2020.06.013.

[53] X.C. Li, Y. Zhang, C.Y. Wang, Y. Wan, W.Y. Lai, H. Pang, W. Huang, Redox-active triazatruxene-based conjugated microporous polymers for high-performance supercapacitors, Chem. Sci. 8 (2017) 2959–2965.

[54] Y. Liao, H. Wang, M. Zhu, A. Thomas, Efficient supercapacitor energy storage using conjugated microporous polymer networks synthesized from buchwald–hartwig coupling, Adv. Mater. 30 (2018), 1705710, https://doi.org/10.1002/adma.201705710.

[55] M.G. Mohamed, S.V. Chaganti, M.S. Li, M.M. Samy, S.U. Sharma, J. Lee, T.M. H. Elsayed, H.H. Chou, S.W. Kuo, Ultrastable porous organic polymers containing thianthrene and pyrene units as organic electrode materials for supercapacitors, ACS Appl. Energy Mater. 5 (2022) 6442–6452, https://doi.org/10.1021/acsaem.2c00942.

[56] M. Boota, C. Chen, M. Bécuwe, L. Miao, Y. Gogotsi, Pseudocapacitance and excellent cyclability of 2,5-dimethoxy-1,4-benzoquinone on graphene, Energy Environ. Sci. 9 (2016) 2586–2594.

[57] M.G. Mohamed, A.F.M. EL-Mahdy, T.S. Meng, M.M. Samy, S.W. Kuo, Multifunctional hypercrosslinked porous organic polymers based on tetraphenylethene and triphenylamine derivatives for high-performance dye adsorption and supercapacitor, Polymers 12 (2020) 2426.
[58] R. Malik, L. Zhang, C. McConnell, M. Schott, Y.Y. Hsieh, R. Noga, N.T. Alvarez, V. Shanov, Three-dimensional, free-standing polyaniline/carbon nanotube composite-based electrode for high-performance supercapacitors, Carbon 116 (2017) 579–590.
[59] Q. Wang, J. Yan, T. Wei, J. Feng, Y.M. Ren, Z.J. Fan, M.L. Zhang, X.Y. Jing, Two-dimensional mesoporous carbon sheet-like framework material for high-rate supercapacitors, Carbon 60 (2013) 481–487.
[60] S.X. Zuo, J. Chen, W.J. Liu, X.Z. Li, Y. Kong, C. Yao, Y.S. Fu, Preparation of 3D interconnected hierarchical porous N-doped carbon nanotubes, Carbon 129 (2018) 199–206.
[61] Q.S. Meng, K.Q. Qin, L.Y. Ma, C.N. He, E.Z. Liu, F. He, C.S. Shi, Q.Y. Li, J.J. Li, N. Q. Zhao, N-Doped porous carbon nanofibers/porous silver network hybrid for high-rate supercapacitor electrode, ACS Appl. Mater. Interfaces 9 (2017) 30832–30839.
[62] L.F. Chen, X.D. Zhang, H.W. Liang, M.G. Kong, Q.F. Guan, P. Chen, Z.Y. Wu, S. H. Yu, Synthesis of nitrogen-doped porous carbon nanofibers as an efficient electrode material for supercapacitors, ACS Nano 6 (2012) 7092–7102.
[63] A.M. Khattak, H. Sin, Z.A. Ghazi, X. He, B. Liang, N.A. Khan, H.R. Alanagh, A. Iqbal, L. Li, Z. Tang, Controllable fabrication of redox-active conjugated microporous polymers on reduced graphene oxide for high performance faradaic energy storage, J. Mater. Chem. A 6 (2018) 18827–18832.